

# Densification of WC-Fe-Ni-Co-Cr cemented carbides processed by HIP after sintering: effect of WC powder particle size

Tomas Soria-Biurrun<sup>a,b,\*</sup>, Lorena Lozada-Cabezas<sup>a,b</sup>, Jazmina Navarrete-Cuadrado<sup>a,b</sup>, Federico Ibarreta-Lopez<sup>c</sup>, Roberto Martinez-Pampliega<sup>c</sup>, Jose M. Sánchez-Moreno<sup>a,b</sup>

<sup>a</sup> CEIT-Basque Research and Technology Alliance (BRTA), Manuel Lardizabal 15, 20018 Donostia/San Sebastián, Spain

<sup>b</sup> Universidad de Navarra, Tecnun, Manuel Lardizabal 13, 20018 Donostia/San Sebastián, Spain

<sup>c</sup> FMD CARBIDE, Fabricacion Metales Duros, S.A.L., Gudarien etorbidea, 18, 48970 Basauri, Spain

## ARTICLE INFO

### Keywords:

WC-Fe-Ni-Co-Cr alloys  
WC powder particle size  
Shrinkage  
Liquid formation  
Carbothermal reduction

## ABSTRACT

Shrinkage, liquid formation and mass losses of WC-19 vol% FeNiCoCr alloys during sintering have been investigated in compositions either with coarse or submicron WC powders. Mass losses detected by thermogravimetry are compatible with carbothermal reduction of the different oxides present in the powder mixtures. Hardness and fracture toughness of materials based on submicron WC powders are within tolerances of those reported for WC-Co materials with similar microstructures. However, fracture strength is approx. 25% lower.

## 1. Introduction

Cobalt partial or total substitution in hardmetals is still an active field of research mainly driven by changes in its classification as toxic substance [1–4] and by the risk of supply associated to its use in Li-ion batteries [5]. Among these alternative cemented carbides, those based on the WC-Fe-Ni-Co system have been extensively studied due to their good sinterability and mechanical properties [6,7]. Moreover, these materials exhibit carbon windows compatible with industrial scale-up, specially when the binder phase solidifies as austenite [8,9]. More complex alloys have also been proposed not only for Co replacement in hardmetals but also for improving their high temperature performance. High entropy alloys (HEA) are one of such potential candidates [10–15]. However, sintering of WC-HEA materials seems to be a challenging task since both thermodynamic studies and sintering experiments confirm the precipitation of undesired phases, like  $M_7C_3$  and other Cr-rich carbides [16–19]. More recent works have shown that Fe-Ni-Co-Cr multi-component alloys are suitable binders for WC based cemented carbides provided that Cr concentrations are below 8 wt% of the total metal content. Under these conditions, the precipitation of  $M_7C_3$  carbides is completely avoided [20]. These has been confirmed for a limited number of compositions based on coarse WC powders. In this work, efforts are focused on analyzing the effect of WC powder particle size on the sintering behavior and mechanical properties of these new WC-Fe-Ni-

Co-Cr alloys. The aim is to explore the versatility of WC-Fe-Ni-Co-Cr materials for obtaining materials with different combinations of hardness and toughness, similarly to that described in WC-Co alloys.

## 2. Experimental procedure

Mean particle sizes of selected powders are included in Table 1 and the compositions of the powder mixtures are given in Table 2.

Alloys 1 and 3 were prepared with the WC coarse grade and alloys 2 and 4 with the WC submicron one. As described in Table 2, the latter was already doped with Cr and V in as-received state. Therefore, alloy 1 is the only one without Cr or V additions. This is already taken into account in Table 2. In all cases, the metal content was  $12 \pm 1$  wt% ( $\approx 19 \pm 1$  vol%) and the ratio between Fe, Ni and Co was 40/40/20 (in wt%). Fe and Ni powders were both from carbonyl-type materials. C and Cr contents were adjusted via carbon black additions in all cases to ensure that the materials were within their corresponding carbon windows [20]. Mixing/milling was made in a planetary equipment at 100 rpm for 5 h using ethanol as liquid media and a ball to powder ratio of 6 (in wt %). Paraffin, used as pressing aid, was added in the last milling hour. Afterwards, the powders were dried for 40 min at atmospheric pressure in a thermostatic bath ( $80 \pm 2$  °C). Green compacts were obtained by double action pressing at 160 MPa. The equipment used in dilatometric experiments was a Netzsch TA 402 E/7 and that used in differential

\* Corresponding author at: CEIT-Basque Research and Technology Alliance (BRTA), Manuel Lardizabal 15, 20018 Donostia/San Sebastián, Spain.

E-mail address: [tsoria@ceit.es](mailto:tsoria@ceit.es) (T. Soria-Biurrun).

<https://doi.org/10.1016/j.ijrmhm.2022.105994>

Received 29 March 2022; Received in revised form 8 August 2022; Accepted 11 September 2022

Available online 15 September 2022

0263-4368/© 2023 The Authors. Published by Elsevier Ltd. This is an open access article under the CC BY-NC-ND license (<http://creativecommons.org/licenses/by-nc-nd/4.0/>).

**Table 1**

Mean particle size of starting powders obtained from FSSS analyses.

Powders	WC-coarse	WC-submicron*	Fe	Co	Ni	Cr <sub>3</sub> C <sub>2</sub>
Mean size (μm)	3.7	0.8	5.3	1.7	1.1	3.9

\* WC submicron powder was already doped with 0.6 wt% Cr<sub>3</sub>C<sub>2</sub> and 0.3 wt% VC.

scanning calorimetric tests was a TGA/DSC Setaram Setsys Evolution 16/18. Dilatometric specimens were cylinders with both height and diameter of 5 mm. DSC samples were cubes of aprox. 1 mm side. The heating cycle was the same in both types of experiments. It consisted of a heating ramp of 10 °C/min up to 1450 °C. Dwelling time at this temperature was 10 min. Argon at atmospheric pressure was used as a protective atmosphere. Temperatures T<sub>i</sub> and T<sub>f</sub> correspond to the upper and lower bounds of the melting range of each DSC peak respectively and were determined by using the SETSOFT software [21]. Peak areas calculated by this software only provide a qualitative estimation of the amount of liquid generated by each DSC peak, since quantitative calculations require knowing the enthalpy of melting of Fe-Ni-Co-Cr-W alloys, which are still unknown. Some DSC experiments were repeated thrice for each specimen in order to compare melting phenomena of

elemental powder mixtures with those of already alloyed Fe-Ni-Co-Cr-W) multicomponent binders.

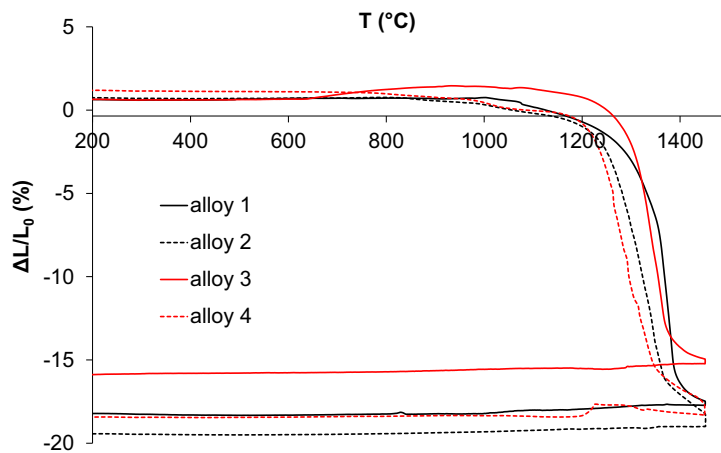
After DSC tests, standard vacuum sintering experiments were carried out in an industrial furnace with graphite heating elements at a heating rate of 10 °C/min up to 1450 °C. The vacuum level used during this step was 10<sup>-2</sup> mbar. After reaching the sintering temperature, the pressure was increased up to 100 mbar by introducing argon in the furnace chamber and maintained during the 1 h sintering plateau. After vacuum sintering, a hot isostatic pressing treatment (HIP) was applied in order to eliminate any residual porosity. HIP cycles were made at 1400 °C and 150 MPa for 1 h.

C contents were measured by means of infrared spectrometry both in green compacts and sintered materials. Green density was calculated from geometric measurements, whereas standard ISO 3369 was used for density measurements in sintered samples. These specimens were ground and polished down to 1 μm diamond paste for microstructural analysis, which was carried out by optical and scanning electron microscopy (FEG-SEM) and energy dispersive X-ray spectroscopy (EDS). Phase identification was carried out by X-Ray diffraction (XRD) (with Ni-filtered CuKα radiation) using Bragg-Brentano configuration. Average WC grain sizes ( $L_w$ ), binder mean free paths ( $L_b$ ) and contiguities ( $C_w$ ) were measured following ISO 4499-2-2020. Vickers hardness was

**Table 2**

Composition of selected WC-Fe-Ni-Co-Cr alloys (in wt%).

Powders	WC-coarse	WC-submicron	Fe	Ni	Co	Cr <sub>3</sub> C <sub>2</sub>	VC	Nominal C content
Alloy 1	88.55	-	4.58	4.58	2.29	-	-	5.43
Alloy 2	-	87.75	4.58	4.58	2.29	0.53	0.27	5.50
Alloy 3	87.83	-	4.59	4.59	2.29	0.70	-	5.47
Alloy 4	-	87.03	4.59	4.59	2.29	1.23	0.27	5.55

**Fig. 1.** Shrinkage vs. temperature corresponding to the four investigated WC-FeNiCoCr alloys.**Table 3**

Microstructural characteristics and mechanical properties of selected WC-Fe-Ni-Co-Cr alloys.

Alloy n°	1		2		3		4	
	VS	HIP	VS	HIP	VS	HIP	VS	HIP
Green density (g/cm <sup>3</sup> )	8.2 ± 0.1		7.2 ± 0.1		8.2 ± 0.1		7.2 ± 0.1	
Density after sinter (g/cm <sup>3</sup> )	13.8	14.2	13.2	14.2	13.6	14.1	12.3	14.0
%T.D.	97.2	100	92.6	100	96.3	99.6	86.7	99.1
C <sub>α</sub>	0.50	0.49	0.63	0.69	0.53	0.47	0.63	0.79
L <sub>w</sub> (μm)	1.43	1.24	0.32	0.33	1.49	1.48	0.31	0.35
L <sub>b</sub> (μm)	0.59	0.53	0.17	0.18	0.49	0.53	0.13	0.24
HV30 (kg/mm <sup>2</sup> )	1101 ± 14	1112 ± 8	1265 ± 63	1615 ± 12	1094 ± 14	1109 ± 24	1165 ± 82	1665 ± 16
K <sub>1C</sub> (MPa m <sup>1/2</sup> )	*	*	8.60	8.10	*	*	8.10	6.90
TRS (MPa)	-	-	-	2696 ± 63	-	-	-	-

\* No cracks are produced by indenting with 30 kg. of applied load.

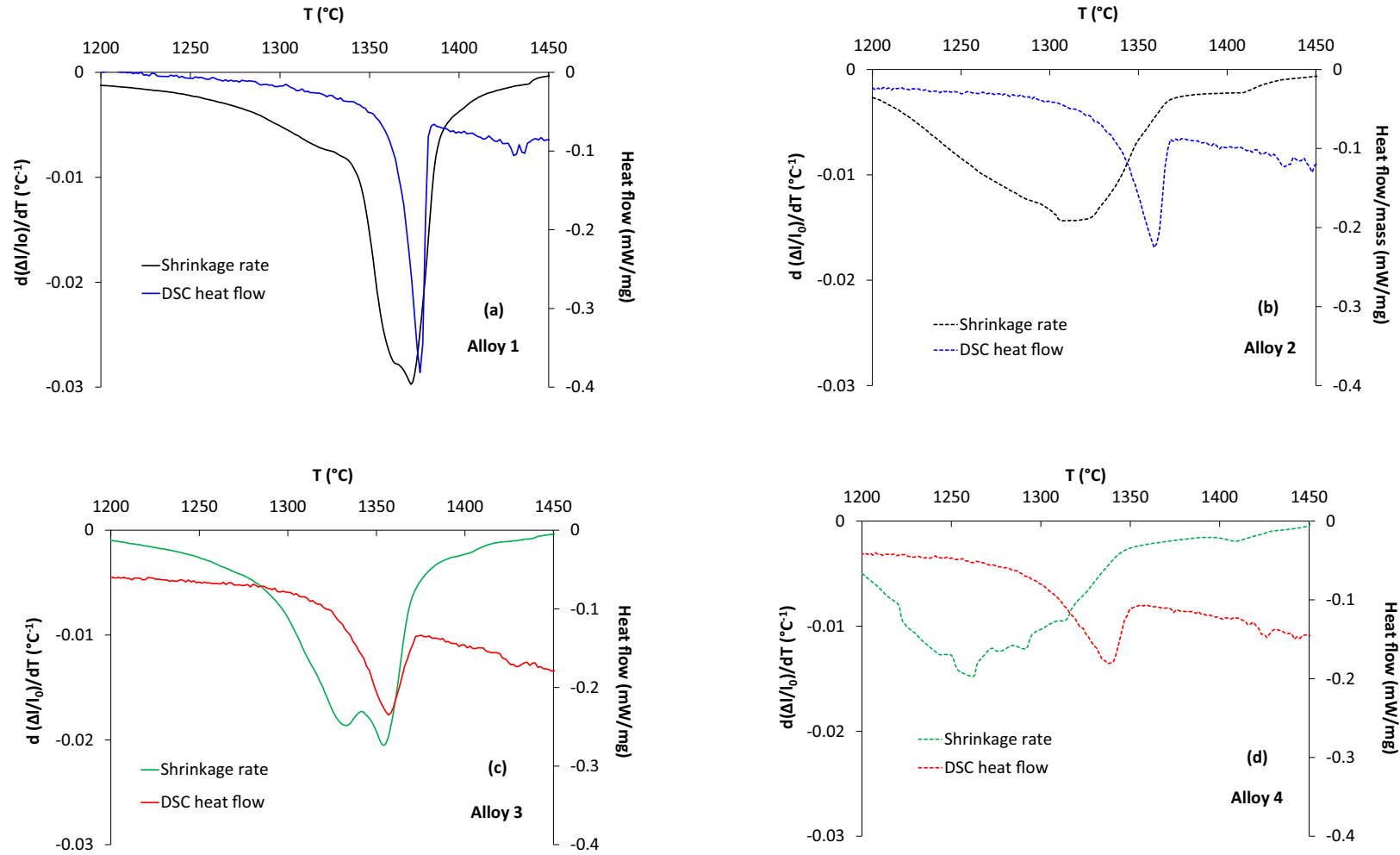


Fig. 2. Shrinkage rate vs. temperature and DSC endothermic peaks corresponding to melting events: (a) alloy 1, (b) alloy 2, (c) alloy 3 and (d) alloy 4.

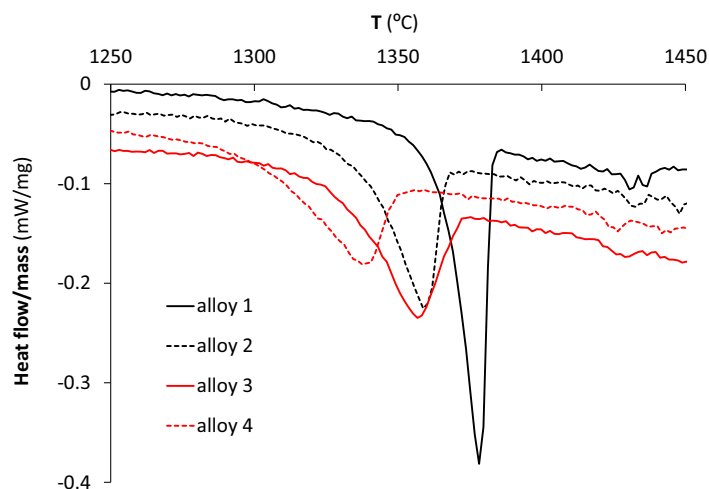


Fig. 3. DSC plots corresponding to alloys 1–4. These data correspond to the first heating ramp.

determined with 30 kg of applied load at room temperature (ISO 3878) and Palmqvist fracture toughness was calculated from the cracks generated by such indentations (ISO 28079:2009) [22]. Finally, the fracture strength of alloy 2 has been measured by applying ISO-3327 on rectangular prisms of  $20 \times 6.5 \times 5.25$  mm (5 specimens per alloy).

### 3. Results and discussion

#### 3.1. Thermal analyses: dilatometry and calorimetry

Dilatometric data confirm that shrinkage is significantly higher for the WC-Fe-Ni-Co-Cr compositions based on finer WC powders (Fig. 1).

This is similar to that described for WC-Co alloys and is mainly due to the lower green density achieved when pressing the mixtures based on finer powders (Table 3) [23]. As all four alloys reach densities close to the theoretical values after sintering, those with lower green densities have to shrink more.

On the other hand, it is observed that additions of  $\text{Cr}_3\text{C}_2$  powders tend to reduce the total shrinkage of WC-FeNiCoCr alloys. This effect is more evident in alloys based on coarse WC powders. Thus, shrinkage is 18% lower for alloy 3 than for alloy 4, whereas this difference is only of 6% between alloys 1 and 2. It is also worth noting that alloy 3 exhibits significant swelling between 740 °C and 1100 °C.

Assuming that shrinkage phenomena before melting are likely related to the diffusion of Fe, Ni and Co atoms towards the surface of WC grains, these results suggest that the resistance to shrinkage depends on the way of adding chromium to the system. When it is added as relatively coarse  $\text{Cr}_3\text{C}_2$  particles, these may either act as physical barriers for such diffusion or modify the diffusivity of the different metallic atoms by their mutual dissolution during heating. On the other hand, when Cr is added to WC powders by doping prior to carburization, this resistance to shrinkage is overcome due to the higher driving force associated to the reduction of the total surface energy of the system.

The effect of the liquid phase on shrinkage is analyzed by comparing shrinkage rate and the DSC peaks (Fig. 2). These data confirm that, in alloys based on submicron doped WC powders (alloys 2 and 4), most of shrinkage occurs in solid state and shrinkage rate is not significantly affected by liquid formation, whereas the opposite is found in alloys based on coarse WC powders (alloys 1 and 3).

Therefore, the shrinkage acceleration observed in alloys 1 and 3 after liquid formation is compatible with particles rearrangement due to capillary forces. However, in alloys 2 and 4, densification in this temperature range is likely controlled by solution-precipitation mechanisms. As described for WC-Co ultrafine grades, these processes are slower and less effective in removing the residual porosity, especially in

the presence of WC grain growth inhibitors as Cr and V [24] (Table 3). This hypothesis is compatible with the higher shrinkage detected in alloys 2 and 4 during the dwelling segment of the sintering cycle. This residual porosity, mainly present in alloys 2, 3 and 4, was completely eliminated by HIP after sintering.

The effect of Cr on melting is better perceived in Fig. 3, where all endothermic DSC peaks corresponding to liquid formation are put together.

As observed in this graph, DSC peaks are wider, less deep and displaced towards lower temperatures as Cr content increases. This is detected not only when Cr is added via  $\text{Cr}_3\text{C}_2$  powders to the mixtures but also when it is done by doping during synthesis of WC powders. This behavior is consistent with that observed in WC-Co- $\text{Cr}_3\text{C}_2$  and TiCN-Ni- $\text{Cr}_3\text{C}_2$  systems [16,24] and suggests that similar eutectic reactions could be taking place in the WC-Fe-Ni-Co- $\text{Cr}_3\text{C}_2$  system. Exothermic DSC peaks detected on cooling correspond to the solidification of the liquid phase after sintering. As observed in Fig. 4, these peaks are 20–40 °C narrower than those of melting.

This difference is likely related to the homogenization of the chemical composition of the binder phase that takes place after reaching the plateau of the DSC cycle at 1450 °C. When DSC cycles are repeated on the same specimens, both endothermic and exothermic peaks are less intense and displaced towards higher temperatures. In addition, a second endothermic peak is detected in all four alloys during the second and third heating ramps at temperatures between 1400 °C and 1440 °C. This behavior is qualitatively consistent with Thermocalc® predictions (Fig. 5), suggesting that progressive decarburization occurs on subsequent heating and cooling events. This is confirmed by the precipitation of  $\eta$  phases in all specimens after reheating (Fig. 6).

Quantitative predictions of carbon windows and temperature ranges for solidification obtained with the abovementioned TC® model for alloys 1 and 3 are not consistent with experimental data (Table 4). No free carbon is found in neither of the two alloys after sintering, although their total carbon content measured by IR spectrometry is higher than the lower bound calculated for such precipitation (Fig. 7). Moreover, the actual temperatures corresponding to the onset and end of melting are too high compared to these predictions. Work is still needed in order to provide enough data for a new assessment of the WC-FeNiCoCr system.

On the other hand, carbon contents measured after HIPing (Table 4) are close to those calculated from the stoichiometry of the carbides used in the powder mixtures (excluding that of the paraffin) (Table 2). Assuming that approximately 0.3 wt% C is lost to the carbothermal reduction of powder oxides, there should be other carbon sources available to explain the final C contents measured in as-HIPed specimens. These could be, for example, the residues of paraffin pyrolysis or

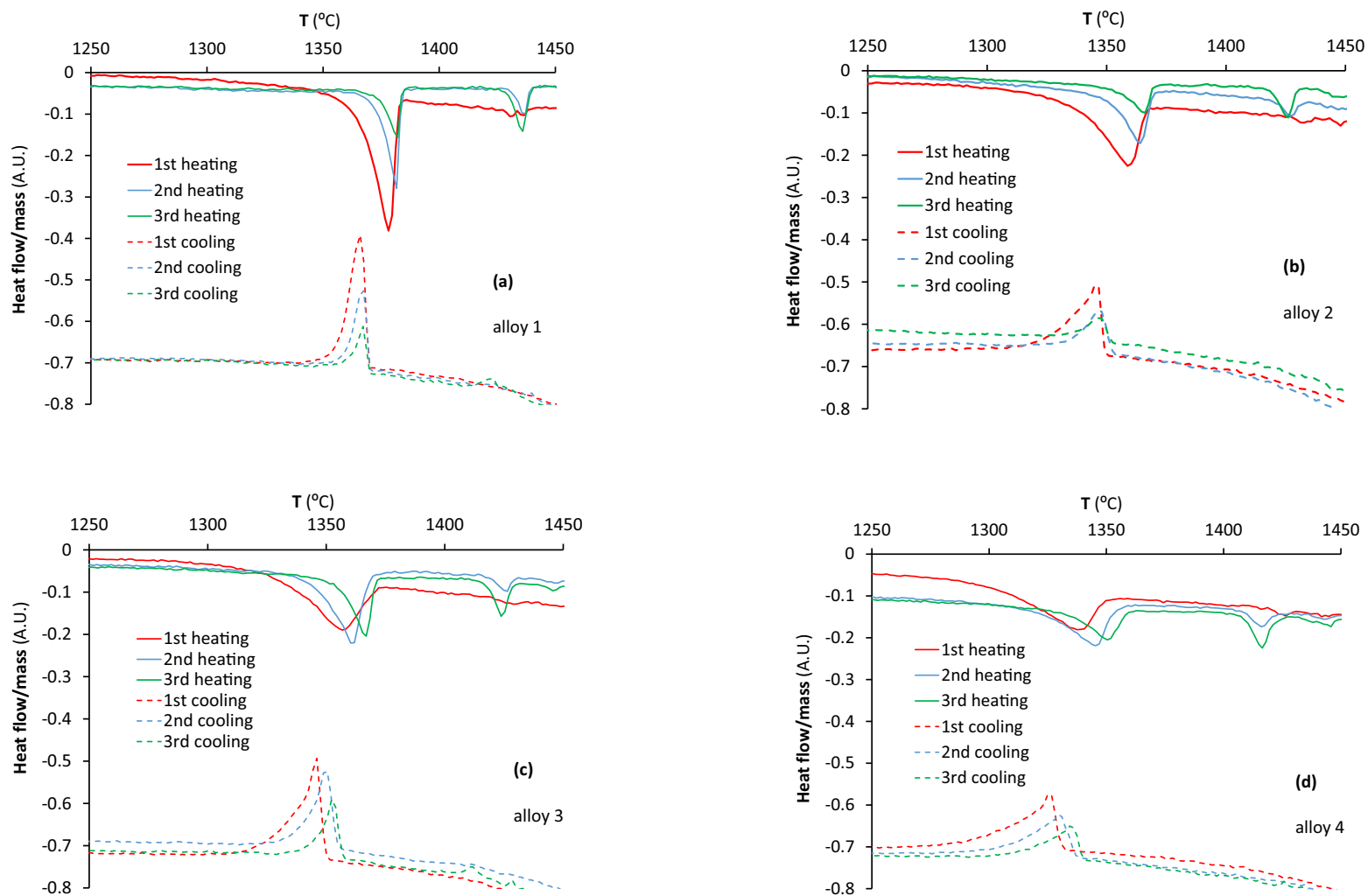


Fig. 4. DSC plots corresponding to repeated heating and cooling cycles: (a) alloy 1, (b) alloy 2, (c) alloy 3 and (d) alloy 4.

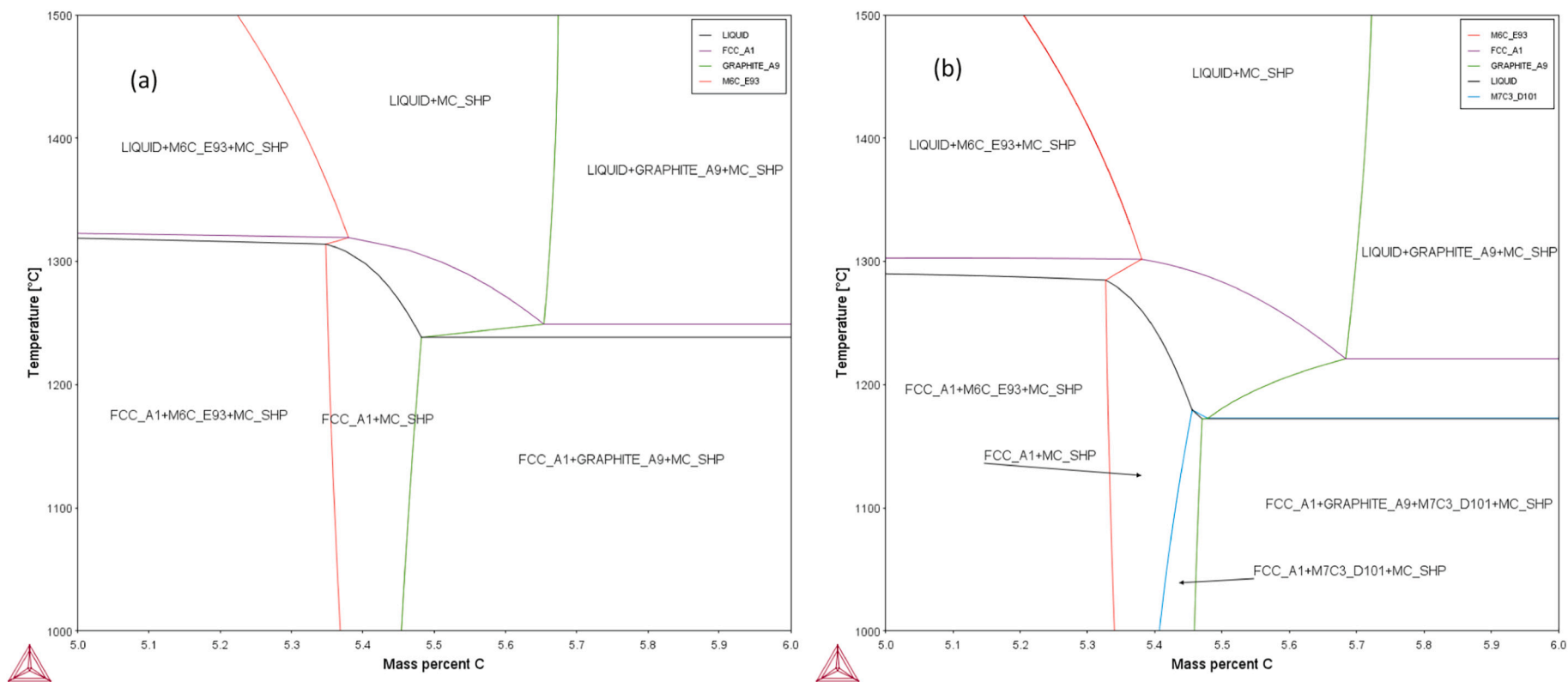


Fig. 5. Isoleths calculated with Thermocalc® software using TCFE10 database corresponding to: (a) alloy 1 and (b) alloy 3.



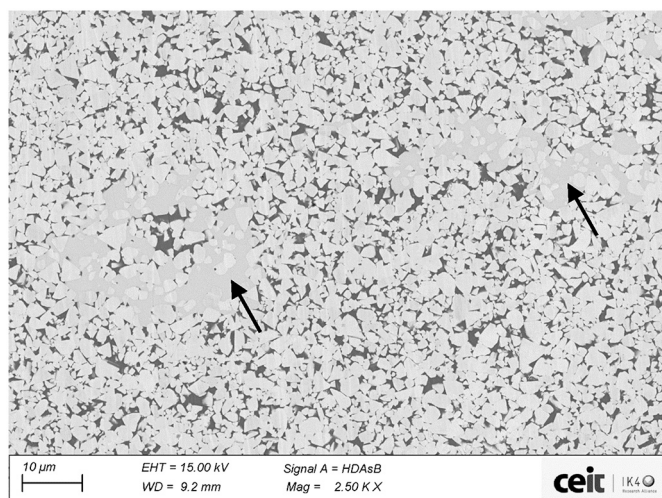


Fig. 6. BSE-SEM image showing the microstructure of alloy 3 after three consecutive DSC cycles. Eta phase regions are pointed by black arrows.

Table 4

Melting ranges and carbon windows calculated by Thermocalc® and TCFE10 database.

Ref.	ThermoCalc® estimates		Temperatures of DSC solidification peaks (°C)		C content * (wt%)
	C window (wt%)	Solidification range (°C)	Onset	End	
Alloy 1	5.37–5.46	1319–1238	1369	1352	5.55 ± 0.03
Alloy 3	5.33–5.45	1302–1179	1352	1318	5.46 ± 0.02

\* Measured in dense specimens by infrared spectrometry.

the C provided by the slight decomposition of the heating elements and the furnace crucible, both made of graphite.

Mass losses measured during the first heating ramp after paraffin burnout are shown in Fig. 8.

These data confirm that mass losses are higher for the grades based on finer WC powders, which is compatible with their higher oxygen contents. The derivatives of these graphs with respect to time show peaks compatible with outgassing phenomena related to carbothermal reduction of the different oxides present in the powder mixtures (Fig. 9 and Table 5). Although actual reactions can be quite complex, a good correlation is found between temperatures calculated for the viability of simple oxide reduction reactions and mass loss rate peaks found in TGA experiments.

Alloy 1, based on coarse WC powders without Cr additions, exhibits 3 mass loss rate peaks at 461 °C, 602 °C and 770 °C (Fig. 8b). The first one is compatible with carbothermal reduction of nickel and cobalt oxides. Temperatures corresponding to  $\Delta G_R = 0$  calculated by Thermocalc® for these reactions differ only by 50 °C, suggesting that both phenomena could overlap during the heating ramp. On the other hand, peaks at 602 °C and 770 °C are consistent with reduction of oxides like Fe<sub>2</sub>O<sub>3</sub>; WO<sub>3</sub> and FeO.

In alloy 2, based on submicron WC powders doped with Cr and V, there are also three mass loss rate peaks at 486 °C, 764 °C and 1000 °C. As described in the previous paragraph, the first peak is likely due to carbothermal reduction of Co and Ni oxides. As the heating ramp continues, a single broad peak is detected between 550 °C and 900 °C. As expected from the higher oxygen content of WC submicron powder, mass losses are mainly due to the reduction of tungsten oxides. The large width of this peak is probably related to overlapping of peaks, since the reduction of Fe<sub>2</sub>O<sub>3</sub> or FeO oxides occur at temperatures just below and above that of WO<sub>3</sub> respectively. The peak detected at 1000 °C is compatible with reactions occurring between chromium oxide and carbon having Cr<sub>3</sub>C<sub>2</sub> or Cr<sub>7</sub>C<sub>3</sub> and CO as products [25]. As seen in Fig. 9, carbothermal reduction of Cr<sub>2</sub>O<sub>3</sub> having Cr and CO as products is only

possible above 1265 °C.

As described in the experimental procedure, alloys 3 and 4 were obtained by adding 0.7 wt% Cr<sub>3</sub>C<sub>2</sub> powders to the mixtures corresponding to alloys 1 and 2 respectively. As alloy 4 is based on Cr–V doped WC powders, its total Cr content is 76% higher than that of alloy 3, but added in a different way. Below 800 °C, these two materials exhibit similar mass loss rate peaks as those described for alloys 1 and 2. Between 450 °C and 500 °C, those associated to carbothermal reduction of Ni and Co oxides and, at temperatures between 500 °C and 900 °C, those corresponding to carbothermal reduction of Fe and W oxides. Above 800 °C, mass losses are much higher for alloy 4 than for alloy 3. This could be consistent with its higher total Cr content. However, oxidation of Cr added by doping to submicron WC does not seem to be very high (see difference between alloys 1 and 2 in Fig. 8a). Moreover, alloys 3 and 4 contain the same amount of Cr<sub>3</sub>C<sub>2</sub> powders and milling conditions have been the same in both cases. The higher content of Cr<sub>2</sub>O<sub>3</sub> oxides in alloy 4 could be explain by considering that Cr<sub>3</sub>C<sub>2</sub> could reduce other oxides present in the compact, like WO<sub>3</sub> or FeO generating additional Cr<sub>2</sub>O<sub>3</sub> as product apart from Fe, W and CO. These reactions have been calculated by Thermocalc® SSUB4 database and are highly exothermic.

### 3.2. Sintering experiments

The scale of microstructural segregation can be estimated from EDS mapping analyses obtained from the surface of green compact in alloy 3 (Fig. 10). These analyses confirm the presence of Fe, Ni and Co agglomerates with sizes ranging from 8 to 20 μm. Fe, Ni and Co agglomerates disappear during the sintering process and form a homogeneous solid solution which spreads surrounding the WC grains. These EDS mapping images also prove that chromium accumulations (corresponding to the added Cr<sub>3</sub>C<sub>2</sub> powder particles) also disappear after sintering, due to their almost total dissolution in the Fe–Ni–Co binder phase (Fig. 11) [20].

SEM images confirm that neither free C nor  $\eta$  phases are present in the sintered specimens (Fig. 7). Twenty alloys with different C contents were prepared in order to define low and high carbon limits. The presence of Cr-rich carbides is very difficult to identify in WC–FeNiCoCr submicron grades. For alloys 2 and 4, the absence of M<sub>7</sub>C<sub>3</sub> or other rich carbides was confirmed up to the resolution level of our X-ray diffractometer. Although the 0.8 μm WC powder particle size in the case of alloys 2 and 4 was almost an order of magnitude smaller than that of the Fe powders (mean size = 5.3 μm), the final distribution of the binder phase after sintering is reasonably homogeneous.

Data included in Table 3 confirm that the alloys 1 and 3 with higher WC grain size, has higher density in vacuum sintering (VS) than alloys 2 and 4 with lower WC grain size. However, all the alloys have porosity levels that are unacceptable and this have an important effect on the density achieved. These results prove that the elimination of the last residual porosity in these alloys is more difficult as the WC grain size decreases and also is related to worse wetting of WC grains. The effect of HIP treatments on the removal of this residual porosity is included in Table 3. Alloy 1 and 2 with 97.2% and 92.6% theoretical density (T.D.) after VS had additional densification after HIPing increased these values up to 100% T.D. However, alloys 3 and 4 with 96.3% and 86.7% T.D. increased this value up to above 99% T.D. On the other hand, when HIP

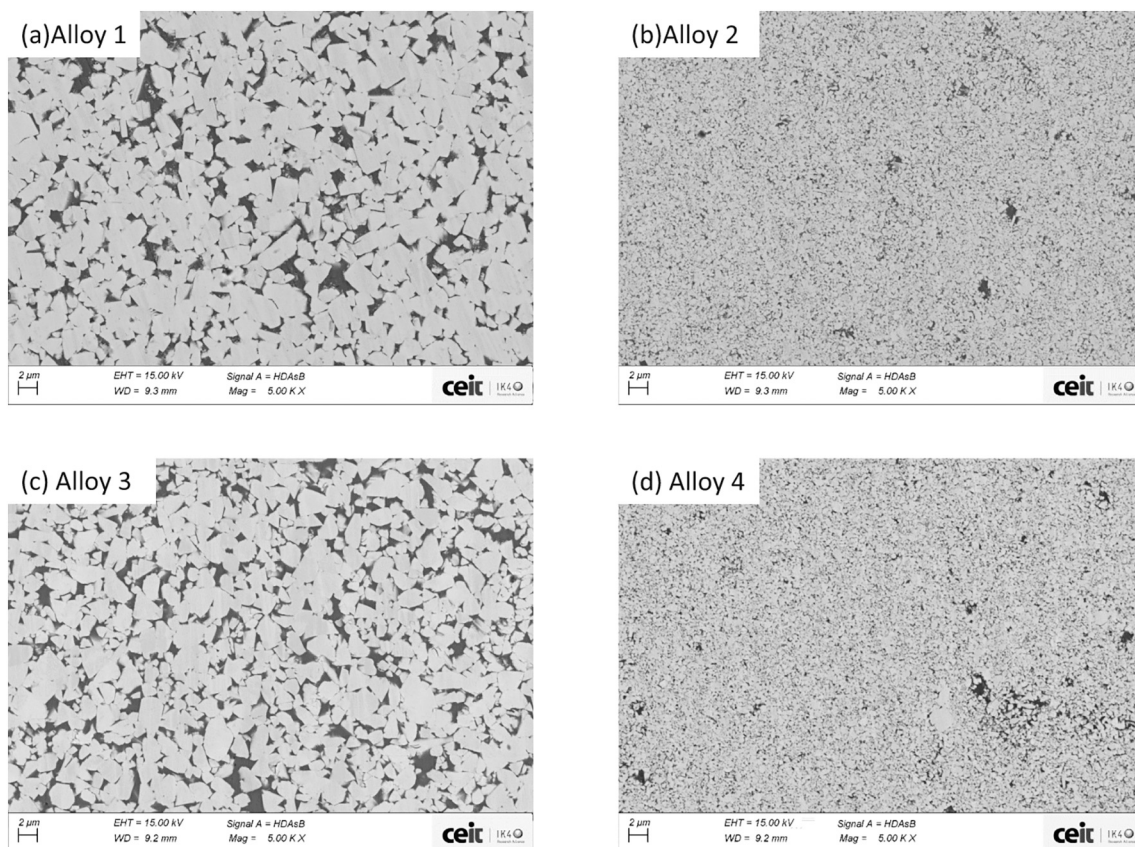


**Fig. 7.** BSE-SEM images showing the microstructure of WC-FeNiCoCr alloys after vacuum sintering followed by HIP treatment: (a) alloy 1, (b) alloy 2, (c) alloy 3 and (d) alloy 4.

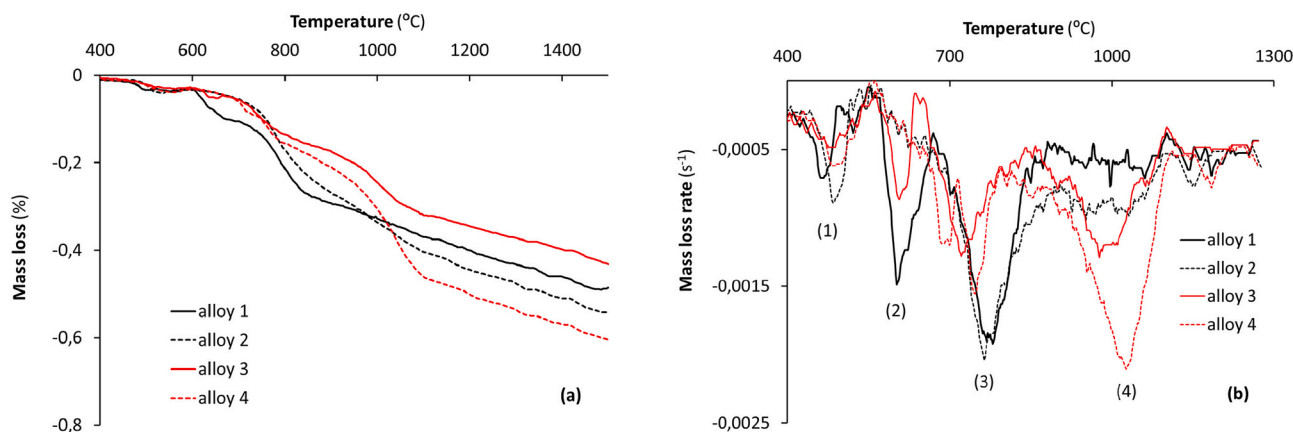


**Fig. 8.** (a) Mass losses detected in WC-FeNiCoCr alloys during the heating ramp of the sintering cycle, (b) mass loss rates obtained by calculating the derivatives of mass loss data with respect to time.

is applied to alloys 1 and 2 densification is more efficient than in the case of alloys 3 and 4. This corroborates that the wetting properties of the liquid are very important in order to remove residual porosity.

As seen in Table 3, there are no large differences between mean WC grain sizes. One reason, in the case of alloys 1 and 3, is that the selected WC powders were already large (that is, the original surface area, which is the driving force for the grain growth process, is low in the starting powders). Moreover, the dissolution of WC grains in Fe based binders is much slower than in Ni or Co based ones [26]. The strong influence of the iron-binder on WC grain growth can be explained as a result of changes in the interface energy of the respective WC/binder interface as well as an increase in activation energy of the interface reaction due to

interactions between the binder atoms with the growth active carbon atoms. This supports the concept of an interface-controlled growth mechanism [27]. This combined with the WC grain growth inhibition effect of chromium additions could explain the rounded morphology found for WC grains in alloy 3. However, alloy 1 (without Cr) show some WC polygonal grains after sintering (Fig. 7). The observed shape change in WC crystals could be due to the activation of 2D nucleation phenomena [26].

Comparing results, it is concluded that for these levels of metallic content, Cr does not affect the overall hardness of the composite material, contrary to that found by other authors for lower metal contents [8]. It would like to point out that the densification obtained after



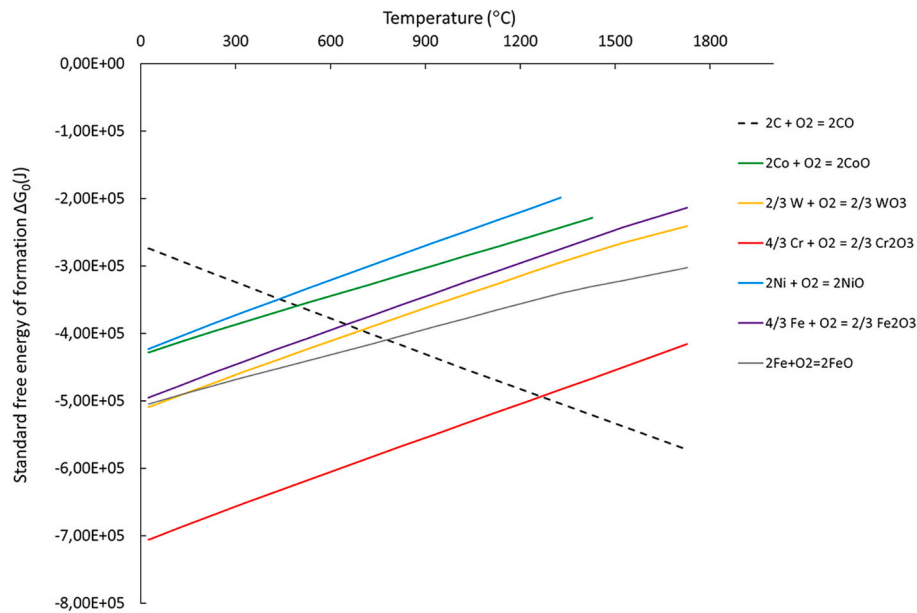


**Fig. 9.** Gibbs energies corresponding to the reactions related to carbothermal reduction of the different oxides present in the WC-FeNiCoCr powder mixtures (Thermocalc® SSUB4 database).

**Table 5**

Mass loss rate peaks and temperatures needed for carbothermal reduction of the different oxides present in the powder compacts.

Reaction	Temperatures for $\Delta G_R = 0$	Mass loss rate peaks (°C)				
		Peak	Alloy 1	Alloy 2	Alloy 3	Alloy 4
$\text{CoO} + \text{C} = \text{Co} + \text{CO}$	450 °C	(1)	461	486	473	490
$\text{NiO} + \text{C} = \text{Ni} + \text{CO}$	500 °C					
$1/3 \text{Fe}_2\text{O}_3 + \text{C} = 2/3 \text{Fe} + \text{CO}$	650 °C	(2)	602	–	607	690
$1/3 \text{WO}_3 + \text{C} = 1/3 \text{W} + \text{CO}$	708 °C	(3)	770	764	746	747
$\text{FeO} + \text{C} = \text{Fe} + \text{CO}$	787 °C					
$1/3 \text{Cr}_2\text{O}_3 + \text{C} = 2/3 \text{Cr} + \text{CO}$	1265 °C	(4)	–	1000	981	1027

HIPing provides higher hardness in all alloys due to the remove of residual porosity. Hardness values of alloys 1 and 3 inside the C windows show values in the range reported for WC-Co coarse grades with similar volume fraction of binder phase (19 vol% Co): from 940 to 1100 kg/mm<sup>2</sup> (HV30). In addition, commercial references of WC-Co (ultrafine grain size and 10–12 wt% Co) show hardness and toughness values of 1600–1675 HV30 and 10.2–10.4 MPa·m<sup>1/2</sup>. This mean that alloys 2 and 4 have hardness values similar to commercial references, but the values of toughness are lower than commercial references.

In the case of alloy 2, TRS values are 25% lower than that particular grade. Crack initiation places have been clearly identified (Fig. 12). As seen in these images, they correspond to abnormally large WC grains. These phenomenon has been already described in ultrafine WC-Co grades [28] and it is also clearly evidenced in WC-FeNiCo materials. The size of this zone consisting of coalesced abnormally large WC grains

is  $l_c \approx 12.5 \mu\text{m}$ . An alternative calculation of  $K_{Ic}$  for alloy 2 can be made by assuming that this defect is a penny shaped microcrack,  $\sigma$  being the TRS value:

$$K_{Ic} = \sigma (2 l_c / \pi)^{1/2} = 7.8 \pm 0.2 \text{ MPa} \cdot \text{m}^{1/2}$$

This value is in good agreement with that obtained from Palmqvist cracks and suggests that this is the key issue to be solved in order to reach TRS values above 3 GPa.

#### 4. Conclusions

WC-19 vol% FeNiCoCr cemented carbides have been obtained from two WC powder grades with mean particles sizes of 3.7 and 0.8  $\mu\text{m}$  respectively. The sinterability of both types of materials is poorer than that of similar WC-Co standard grades. In all cases, vacuum sintered

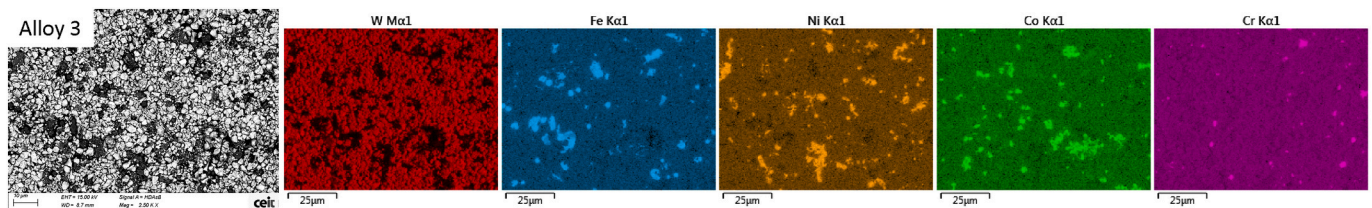


**Fig. 10.** BSE-SEM image corresponding to the surface of green compact of alloy 3 after uniaxial pressing at 160 MPa. EDS mapping images of relevant chemical elements are included to show the degree of segregation of the constituents before sintering. (For interpretation of the references to colour in this figure legend, the reader is referred to the web version of this article.)

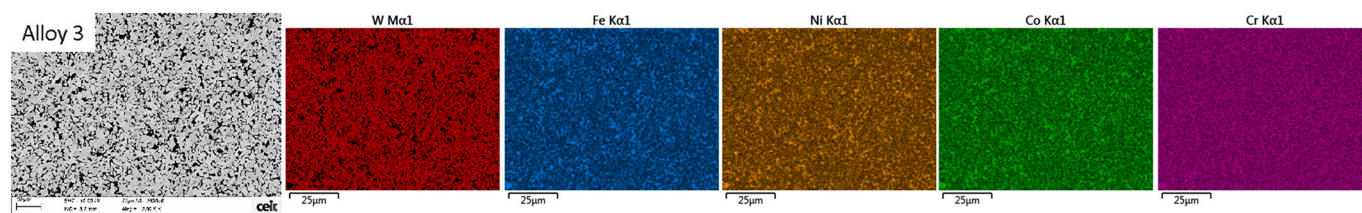


**Fig. 11.** BSE-SEM image showing the microstructure of alloy 3 compact after processing by VS + HIP. EDS mapping images are also included to show the homogeneity achieved after sintering.

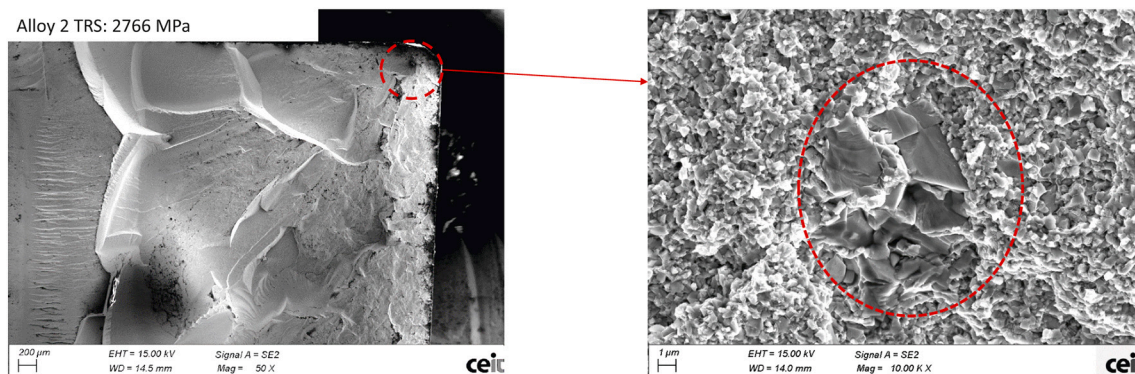


**Fig. 12.** SEM images corresponding to the fracture surface of test specimen of alloy 2 with highest TRS value.

specimens require post-HIP treatments for complete elimination of residual porosity, which is higher as the content of WC grain growth inhibitors increase. As described for WC-Co materials, shrinkage in alloys based on WC submicron powders is control by solid state diffusion mechanisms. On the other hand, liquid spreading by capillary forces is the dominant densification phenomenon in alloys based on coarse WC powders. The introduction of Cr in the W-C-Fe-Ni-Co system induces significant changes in the position of carbon windows and in the solidus and liquidus temperatures with respect to those predicted by ThermoCalc®-TCFE10 database. Mass losses detected during the heating ramp occur at temperatures compatible with those required for carbothermal reduction of the oxides present in the mixtures. Differences are found between coarse and submicron grades, specially above 800 °C. Hardness and fracture toughness of materials where Cr is added by doping are close to those reported for WC-Co materials with similar microstructures. However, strength data are 25% lower.

#### Declaration of Competing Interest

The authors declare that they have no known competing financial interests or personal relationships that could have appeared to influence the work reported in this paper.

#### Data availability

Data will be made available on request.

#### Acknowledgments

Fabricación de Metales Duros S.A.L. FMD CARBIDE, L&L ROTARY SOLUTIONS and CDTI (Centro para el Desarrollo Tecnológico Industrial) are gratefully acknowledged for the financial support of this work. Tomas Soria-Biurrun gratefully acknowledges the Department of Education of Navarra Government for the financial support of his doctoral thesis.

#### References

- [1] REACH. [http://ec.europa.eu/environment/chemicals/reach/reach\\_intro.htm](http://ec.europa.eu/environment/chemicals/reach/reach_intro.htm). Data of access: Nov. 20th 2020.
- [2] P. Wild, A. Perdrix, S. Romazini, J.J. Moulin, Lung cancer mortality in a site producing hard metals, *Occup. Environ. Med.* 57 (2000) 568–573.
- [3] B. Gries, L. Prakash, Acute Inhalation Toxicity by Contact Corrosion — the Case of WC-Co. *Proc Euro PM 2007*, Toulouse, France, 2007.
- [4] S. Bastian, W. Busch, D. Kühnel, A. Springer, T. Meissner, R. Holke, S. Scholz, M. Iwe, W. Pompe, M. Gelinsky, A. Potthoff, V. Richter, C. Ikonomidou, K. Schirmer, Toxicity of tungsten carbide and cobalt doped tungsten carbide nanoparticles in mammalian cells in vitro, *Environ. Health Perspect.* 117 (2009) 530–536.
- [5] P. Alves, D. Blagoeva, C. Pavel, N. Arvanitidis, Cobalt: Demand-Supply Balances in the Transition to Electric Mobility, JRC Science for Policy Report, European Commission, 2018. <https://ec.europa.eu/jrc/en/publication/eur-scientific-and-technical-research-reports/cobalt-demand-supply-balances-transition-electric-mobility>. Data of access: Nov. 20th 2020.
- [6] L. Prakash, A review of the properties of tungsten carbide hardmetals with alternative binder systems, in: H. Bildstein, R. Eck (Eds.), *Proc., 13th Plansee Seminar, Reutte Vol.2*, 1993, pp. 110–120.
- [7] L. Prakash, B. Gries, WC hardmetals with iron based binders, in: L. Sigl, P. Röhhammer, H. Wildner (Eds.), *Proc., 17th Plansee Seminar, Reutte Vol. 2*, 2009, HM 5/1.
- [8] W.D. Schubert, M. Fugger, B. Wittmann, R. Useldinger, Aspects of sintering of cemented carbides with Fe-based binders, *Int. J. Refract. Met. Hard Mater.* 49 (2015) 110–123.
- [9] J. García, V. Collado Ciprés, A. Blomqvist, B. Kaplan, Cemented carbide microstructures: a review, *Int. J. Refract. Met. Hard Mater.* 80 (2019) 40–68.
- [10] F. Zhang, C. Zhang, S.L. Chen, J. Zhu, W.S. Cao, U.R. Kattner, An understanding of high entropy alloys from phase diagram calculations, *Calphad* 45 (2014) 1–10.
- [11] L. Toller, C.X. Liu, E. Holmström, T. Larsson, S. Norgren, Investigation of cemented carbides with alternative binders after CVD coating, *Int. J. Refract. Met. Hard Mater.* 62 (2017) 225–229.
- [12] D. Linder, E. Holmström, S. Norgren, High entropy alloy binders in gradient sintered hardmetal, *Int. J. Refract. Met. Hard Mater.* 71 (2018) 217–220.
- [13] E. Holmström, R. Lizárraga, D. Linder, A. Salmasi, W. Wang, B. Kaplan, H. Mao, H. Larsson, L. Vitos, High entropy alloys: substituting for cobalt in cutting edge technology, *Appl. Mater. Today* 12 (2018) 322–329.
- [14] Y. Zhang, T.T. Zuo, Z. Tang, M.C. Gao, K.A. Dahmen, P.K. Liaw, Z.P. Lu, Microstructures and properties of high-entropy alloys, *Prog. Mater. Sci.* 61 (2014) 1–93.
- [15] J.-W. Yeh, S.-K. Chen, S.-J. Lin, J.-Y. Gan, T.-S. Chin, T.-T. Shun, C.-H. Tsau, S.-Y. Chang, Nanostructured high-entropy alloys with multiple principal elements: novel alloy design concepts and outcomes, *Adv. Eng. Mater.* 6 (5) (2004) 299–303.
- [16] K. Frisk, A. Markström, Effect of Cr and V on phase equilibria in Co-WC based hardmetals, *Int. J. Mater. Res.* 99 (3) (2008) 287–293.

- [17] R. de Oro Calderon, C. Edtmaier, W.D. Schubert, Novel binders for WC-based cemented carbides with high Cr contents, *Int. J. Refract. Met. Hard Mater.* 85 (2019), 105063.
- [18] M. Tarraste, J. Kübarsepp, K. Juhani, A. Mere, M. Kolnes, M. Viljus, B. Maaten, Ferritic chromium steel as binder metal for WC cemented carbides, *Int. J. Refract. Met. Hard Mater.* 73 (2018) 183–191.
- [19] R. de Oro Calderon, A. Agna, U.U. Gomes, W.D. Schubert, Phase formation in cemented carbides prepared from WC and stainless steel powder – An experimental study combined with thermodynamic calculations, *Int. J. Refract. Met. Hard Mater.* 80 (2019) 225–237.
- [20] T. Soria Biurrun, L. Lozada Cabezas, F. Ibarreta Lopez, R. Martinez Pampliega, J. M. Sanchez Moreno, Effect of chromium and carbon contents on the sintering of WC-Fe-Ni-Co-Cr multicomponent alloys, *Int. J. Refract. Met. Hard Mater.* 92 (2020), 105317.
- [21] SETARAM Instrumentation, Setsys evolution 16/18, in: SETSOFT User Manual 39, 2002.
- [22] S. Sheikh, R. M'Saoubi, P. Flasar, M. Schwind, T. Persson, J. Yang, L. Llanes, Fracture toughness of cemented carbides: Testing method and microstructural effects, *Int. J. Refract. Met. Hard Mater.* 49 (2015) 153–160.
- [23] R.M. German, *Powder Metallurgy Science*, 2nd edition, MPIF, Princeton, New Jersey, 1997, p. 278.
- [24] G. Gille, B. Szesny, K. Dreyer, H. van den Berg, J. Schmidt, T. Gestrich, G. Leitner, Submicron and ultrafine grained hardmetals for microdrills and metal cutting inserts, *Int. J. Refract. Met. Hard Mater.* 20 (2002) 3–22.
- [25] L.-M. Berger, S. Stolle, W. Gruner, K. Wetzig, Investigation of the carbothermal reduction process of chromium oxide by micro- and lab-scale methods, *Int. J. Refract. Met. Hard Mater.* 19 (2001) 109–121.
- [26] Z. Roulon, J.M. Missiaen, S. Lay, Carbide grain growth in cemented carbides sintered with alternative binders, *Int. J. Refract. Met. Hard Mater.* 86 (2020), 105088.
- [27] B. Wittmann, W.D. Schubert, B. Lux, WC grain growth and grain growth inhibition in nickel and iron binder hardmetals, *Int. J. Refract. Met. Hard Mater.* 20 (1) (2002) 51–60.
- [28] W.D. Schubert, A. Bock, B. Lux, General aspects and limits of conventional ultrafine WC powder manufacture and hard metal production, *Int. J. Refract. Met. Hard Mater.* 13 (1995) 281–296.